The Astrophysical Journal, 878:96 (13pp), 2019 June 20 https://doi.org/10.3847/1538-4357/ab1eb3

Radiative Torques of Irregular Grains: Describing the Alignment of a Grain Ensemble

Joonas Herranen[1], A. Lazarian[2], and Thiem Hoang[3,4]
[1] Department of Physics, University of Helsinki, Gustaf Hällströmin katu 2, FI-00560 Helsinki, Finland; joonas.herranen@iki.fi
[2] Department of Astronomy, University of Wisconsin, 475 North Charter Street, Madison, WI 53706, USA
[3] Korea Astronomy and Space Science Institute, Daejeon 34055, Republic of Korea
[4] Korea University of Science and Technology, 217 Gajeong-ro, Yuseong-gu, Daejeon, 34113, Republic of Korea
Received 2018 December 19; revised 2019 April 24; accepted 2019 April 27; published 2019 June 18

Abstract

The radiative torque (RAT) mechanism is the most promising way of explaining observed polarization arising from aligned grains. We explore the efficiency of the grain alignment by an anisotropic radiation flow for an extensive ensemble of grain shapes, grain sizes (a), and wavelength (λ). We calculate the distribution of the ratios of the amplitudes of the two major components of the RATs, which is an essential parameter that is used in the theory of RAT alignment in Lazarian & Hoang. While this distribution is different for the different classes of grain shapes that we considered, the most probable values of the parameter are centered in the range of $q^{\max} \sim 0.5$–1.5. The functional form from the calculated RATs is in good agreement with the analytical model. We find that the RAT efficiency scales as $(\lambda/a)^{-2.6}$ for $\lambda \gtrsim 1.8a$, which has a slightly shallower slope than previously found in LH07. This increases the power of predictions obtained with the RAT theory. We also confirm that superparamagnetic inclusions are necessary for achieving high degrees of alignment, and constrain the parameter space describing the requirements for achieving these alignment degrees.

Key words: dust, extinction – methods: numerical – polarization – radiation: dynamics

1. Introduction

Polarization from aligned grains is both an important source of information on magnetic fields in diffuse media and molecular clouds as well as a major impediment in the search for the enigmatic cosmological B-modes. The mystery of grain alignment has been an enduring astrophysical problem since the first detection of aligned grains reported in Hiltner (1949) and Hall (1949). The first theories of grain alignment were suggested shortly after that (Davis & Greenstein 1951; Gold 1952b). Later, quite a number of processes of grain alignment weren discussed in the literature (see Lazarian 2003 for a review), with the legends of astronomy, e.g., Ed Purcell and Lyman Spitzer, working intensively on the problem. Their work clarified many key astrophysical processes, but could not provide a theory of alignment that could explain the polarization observations. Apparently, the approaches explored missed a key element. This missing element was introduced by Dolginov & Mytrophanov (1976a), which was published in the relatively obscure journal *Soviet Astronomy*. This prophetic work suggested that some irregular grains are helical in terms of their interaction with the radiation, i.e., they can scatter different amounts of right-handed and left-handed radiation. As a result, such grains subject to anisotropic radiation are expected to get spun up and aligned. The requirements for the grains to be helical were not defined by the authors, nor were the analytical calculations for the given shape, which they adopted as an example of a helical grain, confirmed by the subsequent studies.[5] Nevertheless, Dolginov & Mytrophanov (1976b) introduced the new idea that changed the direction of the subsequent grain alignment research. Another important lesson from the Dolginov & Mytrophanov (1976b) study was that the approximation of grains by spheroids was missing essential pieces of physics.

The next step in the grain alignment saga was done by Draine & Weingartner (1996, henceforth DW96), where the efficiency of radiative torques (RATs) was calculated using the advanced Discrete Dipole Scattering (DDSCAT) code by Draine & Flatau (1994). This work for the first time demonstrated the strength of RATs. In particular, it was shown that for typical ISM conditions the RATs can spin up grains up to the rotational velocities in excess of any other spin -up mechanism, e.g., the mechanism of spin-up related to the formation of molecular hydrogen over the dust grain surface. The latter was suggested in Purcell (1979) and was considered the dominant process of dust suprathermal rotation. While the work of DW96 brought the RATs to the attention of astrophysics, its deficiency was that the estimates of the grain rotation for the calculations were obtained while ignoring the dynamics of the grains in the beam of radiation. Thus, DW96 provided the upper limits of grain rotation that the RATs can induce. For the alignment mechanism DW96 assumed the classical Davis & Greenstein (1951, see also Spitzer & McGlynn 1979; Purcell 1979) paramagnetic relaxation mechanism. This was consistent only for the isotropic RATs which, however, were ~100 times weaker than the anisotropic torques of the radiation beam.

The problem of the RAT alignment induced by anisotropic radiation was addressed in the subsequent study by Draine & Weingartner (1997, henceforth DW97). That study pioneered many elements that were used in the research that followed. In particular, to describe the complex dynamics of grains subjected to a beam of radiation, the phase trajectories of grains were traced and the attractor and repellor points were calculated. This makes it possible to observe the outcome of the complex grain dynamics as grains interact with anisotropic radiation. The deficiency of this study, however, was that the crucial element of grain dynamics, i.e., the crossover, was disregarded in the analysis. The crossover takes place as the grain slows down, so the value of the angular momentum

[5] In fact, the shape adopted for their calculations was too symmetric to produce any torques (Hoang & Lazarian 2009).

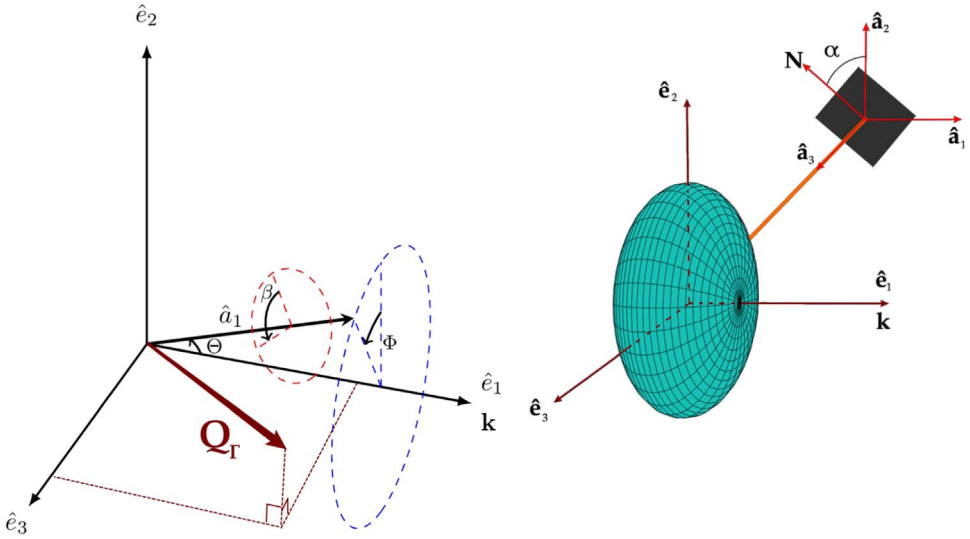

Figure 1. Left: scattering (laboratory) coordinate system, in which β -averaging is done around the axis of the highest moment of inertia $\hat{a}_1(\Theta, \Phi)$. Also, the approximate torque efficiency for a given (Θ, Φ) according to Equation (2) for the right helicity AMO is shown. Right: the mirror-attached-to-spheroid model used to construct AMO. The mirror normal vector $\boldsymbol{N}$ lies in the plane perpendicular to the mirror handle direction $\hat{\boldsymbol{a}}_3$, which is also a minor principal axis of the spheroid. In this image, the spheroid inertia axes coincide with the scattering coordinates.

perpendicular to the grain axis of the maximal moment of inertia gets comparable with the value of angular momentum parallel to the axis of the maximal moment of inertia. The theory of crossovers was suggested by Spitzer & McGlynn (1979) and was extended in Lazarian & Draine (1999).[6] Without the treatment of crossovers in DW97, the obtained grain dynamics was distorted, e.g., the cyclic trajectories were reported for most of the numerical tests. These trajectories happened to be an artifact of the adopted model. The subsequent study in Weingartner & Draine (2003) addressed the issue of crossovers and reported the existence of the attractor points corresponding to a very low angular momentum. This study did not resolve the issue with the cyclic trajectories, which were also presented in the study.

The above studies of the RATs provided the foundations for further progress of the theory. First, it became clear that RATs were an important element of grain alignment theory and they should not be disregarded. Subsequently, ways of calculating the value of RATs and the dynamics of grains were introduced. The deficiency of these studies was that the reason for grain alignment remained unclear and a quantitative theory of grain alignment was still missing. The alignments of grains that corresponded to observations, i.e., with long axes perpendicular to the magnetic field, were tested for a few shapes and the reason why this alignment happens preferentially to the opposite type of alignment, i.e., the alignment with long grain axes parallel to the magnetic field, was unclear.

The set of problems above was addressed in Lazarian & Hoang (2007a, henceforth LH07) where the analytical theory of grain alignment was suggested. The study in LH07 returned to the original idea in Dolginov & Mytrophanov (1976a) that to experience RATs the grains should have intrinsic helicity. However, it proposed a model radically different from the latter study. The Analytical MOdel (AMO) in LH07 employed a macroscopic toy model of a helical grain, which was an oblate grain with a mirror attached to it at 45° to it (see the right panel of Figure 1). The calculations of the torques provided in the framework of geometric optics nevertheless provided remarkable correspondence with the shape of the RATs obtained with the DDSCAT for most of the wavelengths corresponding to the interstellar spectrum. For instance, the model explained the significant differences in the functional dependences of the torques for some of the numerically explored grain shapes. The radical change of the torque shape originated from the helical grains being either left-handed or right-handed. With the AMO, the grain alignment became a predictive theory. LH07 used the abbreviation for RATs, i.e., RATs, which became an accepted term (see Andersson et al. 2015), which we will use for the rest of the paper.

To compare the RATs arising from the AMO and from the DDSCAT calculations, LH07 provided a comparison of torque components in the lab frame that was different from earlier studies. In this frame the component Q_{e3} (see left panel of Figure 1) was found to be present even for spheroidal grains for which both Q_{e1} and Q_{e2} components vanish. The component Q_{e3} was identified along with the cause of the grain precession in the direction of radiation anisotropy.[7] The role of components Q_{e1} and Q_{e2} was explored in LH07 and they were identified as the cause of the RAT alignment. Their functional dependence, i.e., dependence on the angle between the radiation anisotropy direction and the grain axis of maximal moment of inertia (see Figure 1), was shown to be similar to that of AMO. However, the ratio of the amplitude value of the torque components, i.e., $q^{\max} \equiv Q_{e1}^{\max}/Q_{e2}^{\max}$ (see Figure 2) was changing from one irregular grain shape to another. LH07 showed that the properties of alignment, i.e., the alignment with low angular momentum or high angular momentum for a given

[6] Lazarian & Draine (1999) took into account the thermal fluctuations within the grain material (Lazarian 1994; Lazarian & Roberge 1997) and this changed the crossover dynamics, in particular the degree of stochastic randomization from gaseous bombardment during the crossover.

[7] When this precession is faster than the Larmor precession, the grain gets aligned in respect to radiation rather than the ambient magnetic field. This can be termed "*k*-RAT" alignment, as opposed to the "*B*-RAT" alignment with respect to the magnetic field. *B*-type alignment is typical for the interstellar medium, while in the vicinity of bright sources, e.g., stars, novae, and supernovae the alignment can happen with respect to the radiation direction (LH07). This provides an interesting way of measuring magnetic field strength or/and grain magnetic response (Lazarian & Hoang 2018).

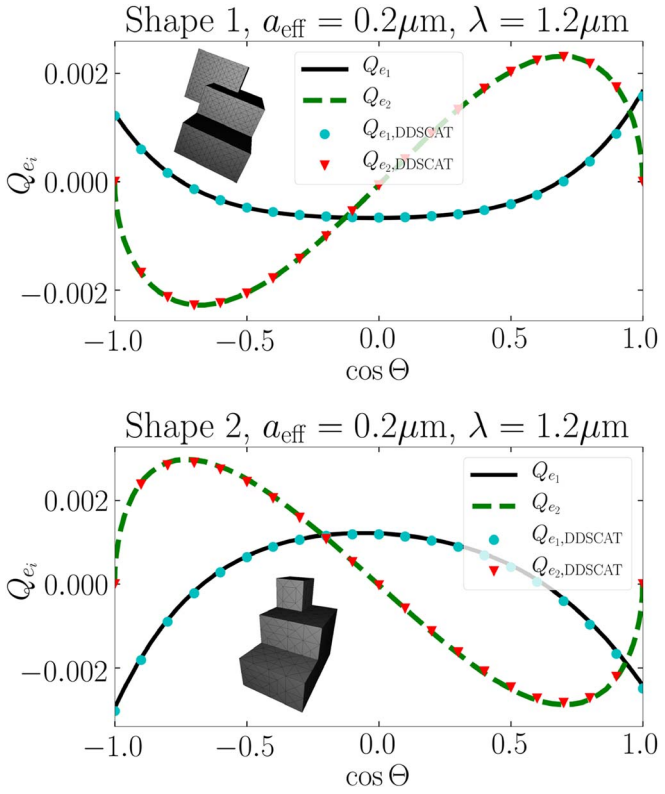

Figure 2. Comparison between the β -averaged torque efficiencies calculated via the *T*-matrix method and DDSCAT for "Shape 1" (top) and "Shape 2" (bottom) of DW97, exhibiting right- and left-handed helicities and $q^{\rm max}$ values 0.72 and 1.0, respectively.

direction between the direction of the magnetic field and the radiation anisotropy, depends on the parameter $q^{\rm max}$. This made $q^{\rm max}$ an essential parameter of RAT theory. While LH07 provided the calculations of $q^{\rm max}$ for the three shapes in DW96 plus additional two shapes, the total number of explored shapes amounted only to five, which precluded any quantitative conclusions on what the expected distribution of $q^{\rm max}$ one should be.

The current study addresses the deficiency of the theory above using contemporary exact light scattering solutions, which have been adapted for use in the dynamical analyses of grains of arbitrary shape composition by Herranen et al. (2017, 2018). The study explores the distribution of $q^{\rm max}$ parameters for a collection of grain shapes of different classes. Our goal is (1) to provide insight into what to expect of the collection of arbitrary shaped grains and (2) provide a way to limit the distribution of grain shapes on the basis of polarization observations.

In what follows, in Sections 2 and 3, we briefly describe the numerical scattering solution and the dust model that are used as the basis of this work. In Section 4, we study the RAT properties of different ensembles and compare the results to those of AMO. We discuss our results in Section 5, and present our conclusions in Section 6.

2. RATs for Irregular Grains

In order to determine the alignment of irregular grains via any quantity describing alignment, two practical issues must be addressed. First, as the properties of interstellar dust are not strictly known, a large set of candidate analogs has to be considered. Second, as RAT alignment is inherently a repeated, dynamically changing scattering problem, an efficient numerical solution is essential. In this section, these issues are considered.

2.1. The T-matrix Solution of RATs

The *T*-matrix method, originally formulated by Waterman (1965), describes electromagnetic scattering in a concise manner. The shape, composition, and size information of the scatterer are encoded in the *T*-matrix, which maps the incident radiation into scattered radiation in the vector spherical wavefunction expansion.

As the properties of the scatterer are described strictly by the *T*-matrix, with no restrictions on the incident radiation direction of beam shape, a repeated solution of scattering by an unchanging scatterer is efficient in the *T*-matrix formulation. In recent years, methods of finding the *T*-matrix of arbitrary scatterers have been developed. This makes it a viable method when considering alignment of irregular grains. In this work, the *T*-matrices are determined via a volume-integral equation approach (Markkanen et al. 2012; Markkanen & Yuffa 2017).

Generally, under anisotropic radiation fields, the RAT $\Gamma_{\rm rad}$ can be defined as

$$\boldsymbol{\Gamma}_{\rm rad} = \frac{\bar{u}_{\rm rad} a_{\rm eff}^2 \bar{\lambda}}{2} \gamma \boldsymbol{Q}_\Gamma(\Theta, \beta, \Phi), \quad (1)$$

where the radiation environment is described by its radiation anisotropy degree γ, the mean wavelength $\bar{\lambda}$, and mean energy density $\bar{u}_{\rm rad}$, $a_{\rm eff}$ is the equivalent volume sphere radius of the grain, and $\boldsymbol{Q}_\Gamma$ is the torque efficiency for a given orientation. The orientation of the grain is described by angles Θ, Φ, and β, where Θ and Φ give the direction of the axis of maximal inertia a_1 with respect to the propagation direction $\boldsymbol{k}$ of the anisotropic radiation, while β is defined as the rotation angle of the grain about a_1. The angle definitions are illustrated in the left panel of Figure 1. In the *T*-matrix framework, the RAT $\Gamma_{\rm rad}$ can be directly written in an analytical form, as a function of the total fields (Farsund & Felderhof 1996).

2.2. Describing the RAT Alignment

An important quantity describing grain alignment is the ratio $q^{\rm max}$, or the q-factor. The q-factor is given by $Q_{ei}^{\rm max}$, $i = 1, 2$, which are maximal magnitudes of the β-averaged RAT efficiency components in the scattering coordinates. The scattering coordinate system allows a decomposition of RAT efficiency as

$$\begin{aligned}\boldsymbol{Q}_\Gamma(\Theta, \beta, \Phi) = {} & Q_{e1}(\Theta, \beta, 0)\hat{\boldsymbol{e}}_1 \\ & + Q_{e2}(\Theta, \beta, 0)(\hat{\boldsymbol{e}}_2 \cos\Phi + \hat{\boldsymbol{e}}_3 \sin\Phi) \\ & + Q_{e3}(\Theta, \beta, 0)(\hat{\boldsymbol{e}}_3 \cos\Phi - \hat{\boldsymbol{e}}_2 \sin\Phi). \quad (2)\end{aligned}$$

The coordinate system is illustrated in Figure 1. For the remainder of this work, RATs are calculated by averaging over β and setting $\Phi = 0$. The q-factor has been identified as an important measure of alignment in LH07. The dominantly aligning component affects what kind of attractor points the grain has in its alignment phase space. In the alignment phase space, we often measure the angular momentum $\boldsymbol{J}$ against the angle between a relevant quantity and the angular momentum vector $\boldsymbol{J} \| \hat{\boldsymbol{a}}_1$, assuming perfect rotation about the maximal inertial axis. In the left panel of Figure 1, the relevant quantity

Table 1
The Generating Parameters, Axial Ratio, Correlation Length l, and Standard Deviation σ, for Each Base Shape

Base Shape	Axial Ratio	l	σ
Ellipsoid	1:0.8:0.6	0.35	0.125
Prolate spheroid	1:0.5:0.5	0.35	0.125
Oblate spheroid	1:1:0.5	0.35	0.125
Sphere	1:1:0.99	0.35	0.125

Note. Fifteen different deformed shapes are generated with a seed index 1–15 for each base shape.

is the radiation direction $\boldsymbol{k}$, and then the angle is Θ. Namely, when Q_{e1} dominates, or $q^{\max}$ is larger than unity, grains have high-J attractor points at $\Theta = 0$. Otherwise, the points are repellors, and the only attractors are low-J at $\Theta = \pi/2$. In addition, when magnetic fields are included, the low-J-only alignment is very probable for grains with $q^{\max} \approx 1$.

The T-matrix method can reproduce previous DDSCAT results from LH07, which is illustrated in Figure 2 for shapes labeled "Shape 1" and "Shape 2," composed of "astronomical silicate" (Draine & Lee 1984). Using 21 angles between 0 and 2π for β, and between 0 and π for Θ in DDSCAT gives torque efficiencies that are accurately (relative differences mostly well within 5% with absolute differences being in order of 10^{-6}–10^{-5}) reproduced by the T-matrix method. A table of the absolute values compared between the two methods is in the Appendix. A more thorough comparison between the methods is provided by Herranen et al. (2017). In order to guarantee good reproducibility with other methods, e.g., DDSCAT, the results of Herranen et al. (2017) suggest that grain models be of the order of 10,000 similarly sized tetrahedra. This ensures that multiple tetrahedra will fit into a single wavelength. As the grain shape models considered in this work contain 20,000–40,000 tetrahedra of comparable volume, and the smallest wavelength is 120 nm, while the largest grain has $a_{\rm eff} = 0.2\,\mu$m, good reproducibility is expected.

3. Model Dust Grain Ensemble

The compositions and shapes of interstellar dust grains are both essentially open, yet still observationally constrained questions. In this work, we assume that extreme aspect ratios are not likely, and consider grain shapes that are deformed randomly from basic shapes in a statistically well-defined manner, which can be especially useful when considering solutions to inverse problems due to the small amount of shape-defining statistical parameters. The compositions are obtained from a publicly open dust model database, THEMIS (Jones et al. 2017).

The T-matrices have been calculated for four ensembles of Gaussian random ellipsoids (Muinonen & Pieniluoma 2011), with their base shapes being spherical, ellipsoidal, oblate spheroidal, and prolate spheroidal. The generating parameters, which are chosen to generate deformed, but not extremely deformed shapes, are summarized in Table 1. Each base shape is deformed 15 different times with a lognormally distributed radius drawn from the same underlying Gaussian random statistics, defined by the correlation length l and standard deviation σ as in Muinonen & Pieniluoma (2011), and different

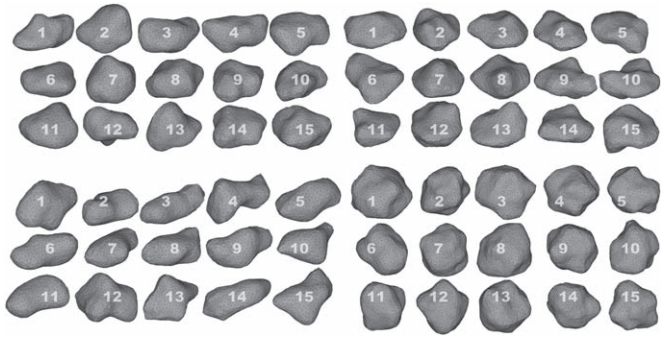

Figure 3. Gaussian ellipsoids, oblate spheroids, prolate spheroids, and spheres, respectively, from the upper left to the bottom right in numbered groups of 15. The numbering also corresponds to the generating indices of the shapes and will be used to identify particles later in the text.

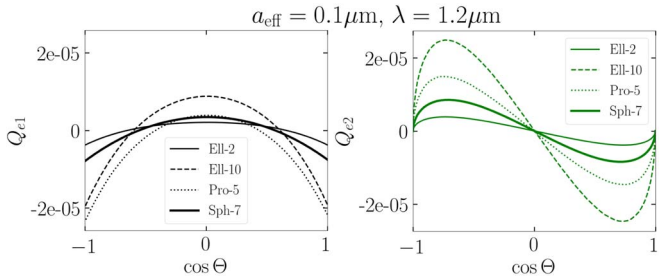

Figure 4. Left-handed RAT components Q_{e1} and Q_{e2} for five random coated silicate shapes for $\lambda = 1.200\ \mu$m.

random seeds. In total, 60 grain shapes are generated. The shapes are illustrated in Figure 3.

For each shape, the T-matrices are calculated for 10 different wavelengths (linearly spaced between 0.120 and 1.740 μm), 3 different particle sizes ($a_{\rm eff} \in \{0.05,\ 0.1,\ 0.2\}\ \mu$m), and 10 different compositions. In this work, a pyroxene-type silicate with a small mantle of carbonaceous material is considered to compose all the grains, unless otherwise stated. The optical properties are available from Jones et al. (2017) and references therein.

To see how the functional forms of the RAT components Q_{e1} and Q_{e2} behave, we consider five random shapes from the 0.1 μm ensemble at $\lambda = 1.2\,\mu$m. Figure 2 shows the characteristic features, helicity differences, and the approximate zeros of the β-averaged Q_{e2} component predicted by AMO. The shape of the torque efficiency of a grain with right-handed helicity can be reproduced by a mirror orientation in AMO that forces the grain to rotate in a clockwise manner when the major inertia axis is parallel to the radiation propagation direction, i.e., when $Q_{e1} > 0$ as $\cos\Theta = \pm 1$. The zeros of Q_{e2} of AMO are then found where the major inertia axis a_1 is either parallel or perpendicular to the radiation beam, i.e., when the mirror cannot induce rotation about $\hat{\boldsymbol{a}}_2$ given that $\Phi = 0$. These features both also appear with the random shapes, as seen in Figures 4–8. The functional form of RATs deviates from those of AMO when the size parameter $x = 2\pi a_{\rm eff}/\lambda$ grows, as expected for irregular grains that are comparable in size or bigger than the incident wavelength. For example, in Figure 4, where $x \approx 0.5$, the RATs are practically identical to those of AMO presented in LH07.

When the size parameter grows, the grain helicities may become more ambiguous as both left- and right-handed helicities are exhibited. This is exemplified in Figures 7 and 8, which

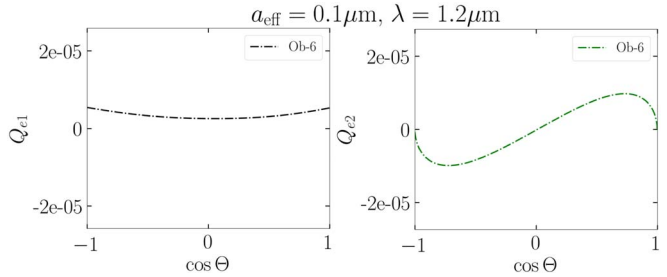

Figure 5. Same as Figure 4, but for the right-handed components.

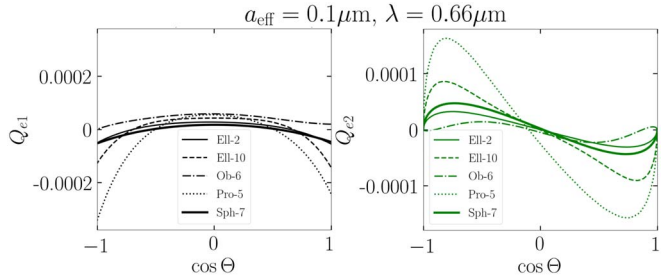

Figure 6. Same as Figure 4, but for $\lambda = 0.660\ \mu$m. All grains show left-handed helicity in this case.

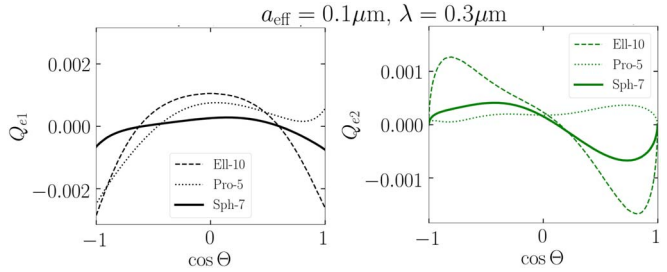

Figure 7. Same RAT components as Figure 4, but for $\lambda = 0.3\ \mu$m, with grains exhibiting mostly left-handed helicity. The prolate grain 5 transitions to right-handed helicity when the major principal axis is nearly parallel to the incident radiation direction.

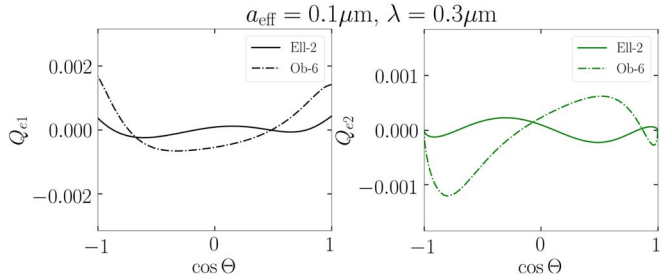

Figure 8. Same RAT components as Figure 5, but for $\lambda = 0.3\ \mu$m, with grains exhibiting a more right-handed helicity. The ellipsoidal grain 2 has helicity transitions when the major principal axis is nearly perpendicular to the incident radiation direction.

correspond to size parameter $x \approx 2$. RATs of randomly deformed shapes can deviate clearly from those of AMO in certain cases when $x > 1$, which was not shown to be as pronounced by the irregular shapes in LH07.

The transition of helicity implies that when grains are both left- and right-handed, different wavelengths may see certain shape features differently. The total handedness is not expected to change for a constant shape. The absolute magnitudes of the RAT components in Figures 4 and 5 show that the shapes

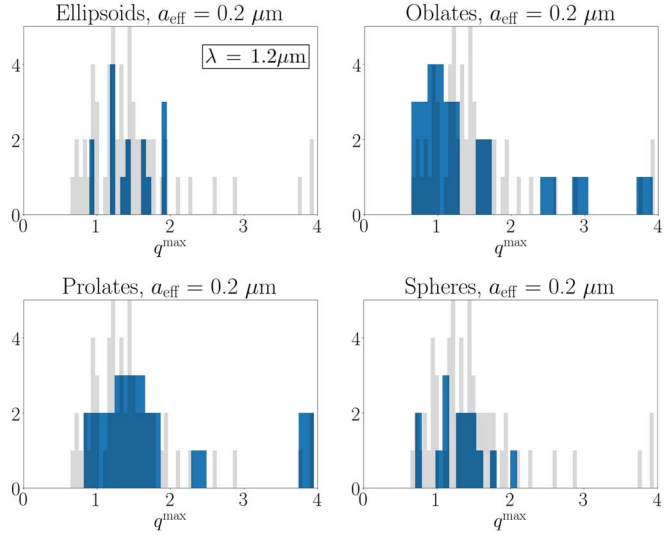

Figure 9. q-factor distributions of different shapes (in dark blue) overlaid with the total distribution of all shapes (in gray). The major spread for all particles is approximately the same, with the spheroids deviating the most.

whose handedness varies with the wavelength also have the smallest RAT efficiencies. Thus, in these cases even small deviations from AMO can introduce change in the interpreted handedness.

From the visible shapes of the RAT components, we can see that the q-factor varies around unity for many shapes with some outliers, such as the prolate spheroid in the $\lambda = 0.3\ \mu$m case. It is cumbersome to analyze the functional forms of a larger amount of particles at once. Thus, in the next section, we probe the statistical behavior of the q-factor for the whole ensemble.

4. Analysis of RATs for the Ensemble

An ensemble of randomly deformed basic shapes allows the collection of q-factor statistics. The shape and composition both affect the distribution of the q-factor. This in turn determines, how effective the alignment without superparamagnetic inclusions will be for different ensembles. In this section, we find distributions of the q-factor for differently shaped and composed ensembles.

4.1. Effect of Shape

First, we compare the effect of shape on the $0.2\ \mu$m ensemble with $\lambda = 1.2\ \mu$m. The distributions are illustrated in Figure 9. All distributions besides the prolate shape are centered around $q = 1.3$–1.4, with the prolate distribution centered at $q = 1.75$. The statistics of this distribution are collected in Table 2.

Distributions of $q^{\rm max}$ such as those in Figure 9 would constrain the grain dynamics in the ISRF considerably. As presented in LH07, $q^{\rm max} \in (0.5,\ 2)$ indicates that high-J attractors are unlikely. In this case, a high degree of alignment could only be produced by enhancement effects such as superparamagnetism.

Motivated by the analyses above, we also consider all differently sized ensembles under ISRF illumination. The simplified ISRF spectrum consists of a 5800 K blackbody intensity spectrum, 10 wavelengths linearly spaced between 120 and 1740 nm with a peak in the 120 nm ultraviolet component. The ultraviolet peak is one-fourth of the peak of

Table 2
Mean, Median, and Standard Deviation of $q^{\max}$ for the 0.2 μm Ensemble with $\lambda = 1.2$ μm for Each Shape

Shape	Mean	Median	STD
Ellipsoid	1.4461	1.4140	0.3333
Oblate	1.4925	1.2450	0.8913
Prolate	1.7583	1.4842	0.8926
Sphere	1.308	1.3228	0.3528
Total	1.5013	1.3601	0.6952

Note. For each row except total, $N = 15$.

the blackbody spectrum. The RAT efficiencies are scaled relative to these intensities when determining the $q^{\max}$ values. For these parameters, the 0.2 μm distributions other than that of prolate shapes are centered around unity. Again, the prolate distribution is centered closer to 2, as is illustrated in Figure 10.

In Figures 11 and 12, the 0.1 and 0.05 μm ensembles are considered. These figures also display the trend in which the prolate shape has distributions that are centered more to the right. However, the 0.05 μm ensemble has the most spread out distributions and all distributions are centered more rightward than the larger grain ensembles. The smallest grains are expected to exhibit AMO-like RATs in the visible and IR wavelengths. Thus, only the 120 nm and 300 nm wavelengths are most likely to give rise to irregular RATs, as seen in, e.g., Figure 8. This would, after averaging the RATs, result in a larger spread of $q^{\max}$ for smaller grains, as is now seen in Figure 12. The statistics of these ISRF distributions are collected in Table 3.

4.2. Effect of Composition

In the total ensemble, there exist five types of grains: pyroxene and olivine type silicates (Scott & Duley 1996) with a thin carbon mantle (Jones 2012), silicates with a thicker carbon mantle, variants of previous grains with 7% iron inclusions (Ordal et al. 1983, 1985, 1988) in the silicate core, and amorphous carbon grains. In general, the iron silicates push the real part of the refractive index higher and widen the imaginary part peak in the ultraviolet. Furthermore, amorphous carbon has a naturally high and wide absorption peak in its refractive index. All analysis in this section is done using the aforementioned simplified ISRF spectrum.

While iron inclusions severely affect the superparamagnetic properties of grains, they do not significantly change the calculated q-factors. This is demonstrated in Figure 13, where the distributions of grains with and without inclusions are nearly identical. Thus, all silicates can be differentiated only by their mantles in this study, leaving three main groups: silicate, carbon-coated silicate, and fully carbonaceous grains.

Comparison between these grain groups in Figure 14 reveals a significant change of $q^{\max}$ distribution for the 0.05 μm ensemble when the amount of carbon is large. However, in the case of larger particles, the effect is less notable, while the tendency of the distribution to shift to larger values when adding carbon still exists. This is again probably due to the averaging of a more limited amount of RATs with irregular behavior. In order to constrain the possible compositions of grains in observations, a more complete study over wavelengths is needed. Indeed, if such a spread of $q^{\max}$ values would

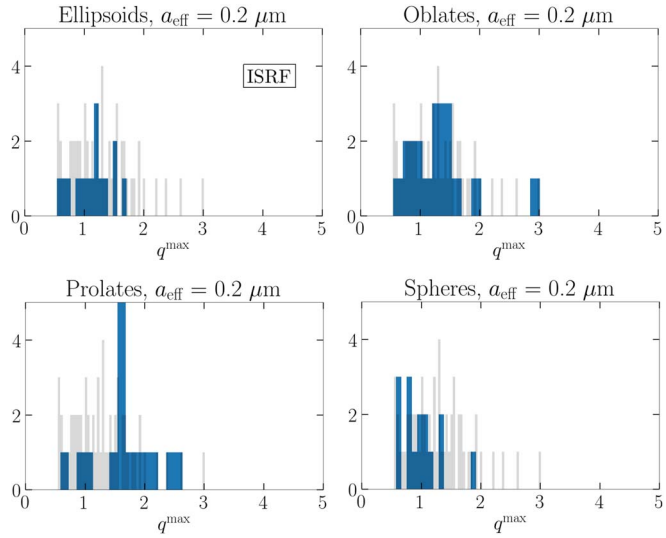

Figure 10. Same as Figure 9, but for the ISRF spectrum.

persist in a more realistic incident field, alignment degrees could in some cases constrain the compositions.

The most probable q-factor falls in the range $q^{\max} = 1.1$–1.5 for the two larger grain ensembles regardless of composition and varies from 1.9 to 3.3 for the 0.05 μm ensemble. Total statistics are collected in Table 4.

4.3. Comparison with AMO

Using the ensemble, a more extensive RAT component comparison between arbitrary grain shapes and AMO can be obtained to justify the model. We thus proceed as in LH07.

First, we compare the effect of both shape and composition on $q_{\max}$ as a function of $\lambda/a_{\rm eff}$, or the ratio of wavelength and effective size of the grain. The mean values and the coefficient of variation of $q^{\max}$ are illustrated in Figures 15–17.

In almost all the cases, the 0.1 μm grains have peaks in $q^{\max}$ near $\lambda/a_{\rm eff} = 3$. Namely, only the peak of the prolate shape, regardless of shape, reaches high-J values. The general downward trend is proportional to $(\lambda/a_{\rm eff})^{-1/2}$, as predicted in LH07, for the oblate and prolate spheroidal Gaussian ellipsoids. Table 5 summarizes the power-law indices for best least-squares fits for all shapes and compositions. Both carbon-coated silicate grains and purely carbonaceous grains also exhibit some relatively strong deviations from the trend for both prolate spheroids and spherical shapes. Altogether, the best fit varies between each test case, but for the non-spherical Gaussian ellipsoids a general power-law fit would be close to −0.5. These data complement the observations in, e.g., Figure 14, where pure 0.05 μm silicates have a highly different distribution from ensembles containing carbon, as can be seen from the difference peaking of 0.05 μm data between Figures 15–17.

Second, we perform $\langle\Delta^2\rangle$ testing between the ensemble and AMO, where $\langle\Delta^2\rangle$ gives the mean deviation of RAT components over Θ as in LH07:

$$\langle\Delta^2\rangle(Q_{ei}) = \frac{1}{\pi(Q_{ei}^{\max})^2}\int_0^{\pi}[Q_{ei}^{\rm irreg} - Q_{ei}^{\rm AMO}]^2 d\Theta. \quad (3)$$

Grain shape has a large effect on the deviation for both RAT components, as illustrated in Figures 18 and 19 for silicates only, as composition does not visibly affect the deviation

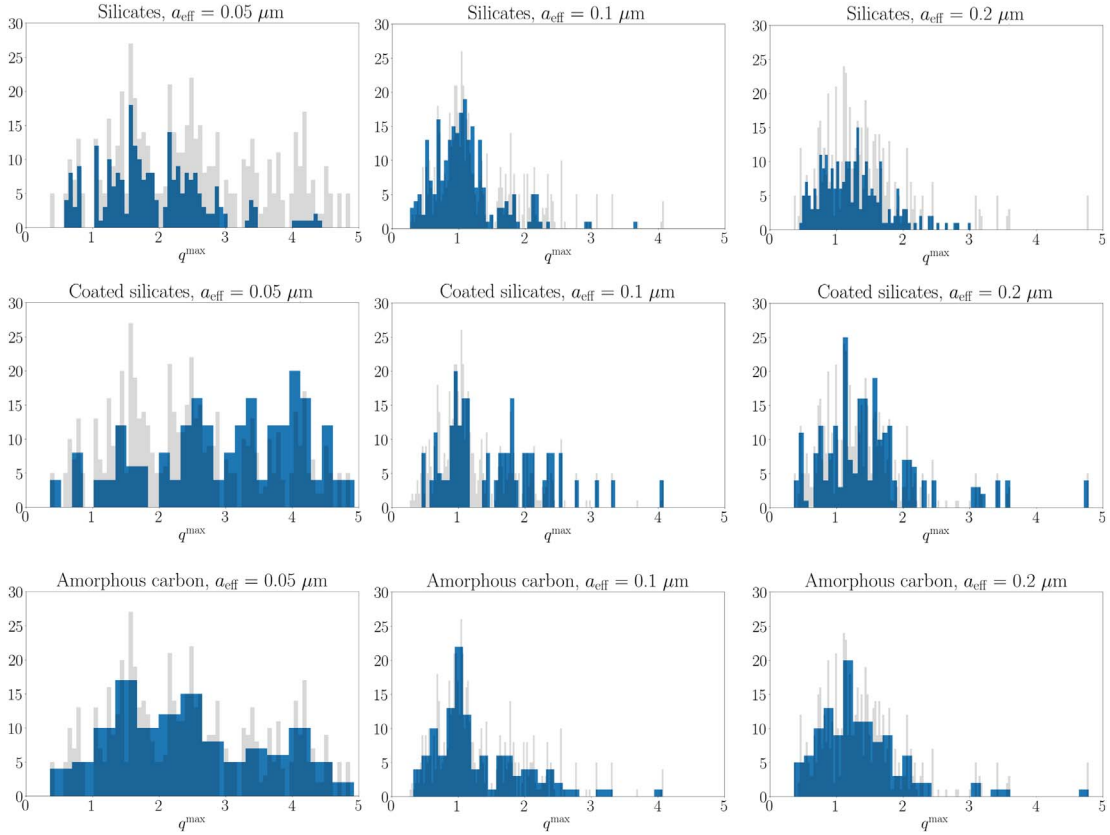

Figure 11. Same as Figure 10, but for the 0.1 μm ensemble.

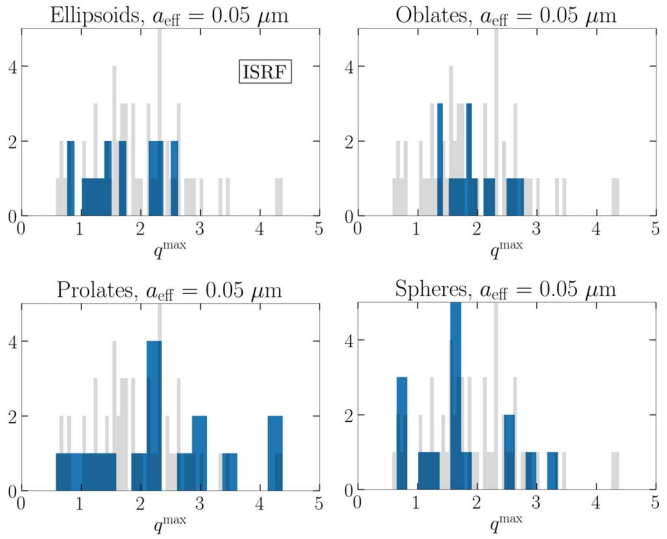

Figure 12. Same as Figure 10, but for the 0.05 μm ensemble.

Table 3
Same as Table 2, but for All Sizes and with the Simplified ISRF Spectrum

Size(μm)	Shape	Mean	Median	STD
0.05	Ellipsoid	1.7040	1.6783	0.5983
0.05	Oblate	1.9307	1.8740	0.4365
0.05	Prolate	2.4061	2.3276	1.0637
0.05	Sphere	1.7012	1.6471	0.7706
	Total	1.9355	1.8117	0.8068
0.1	Ellipsoid	1.0283	0.9496	0.4228
0.1	Oblate	0.9438	0.8650	0.3294
0.1	Prolate	1.2758	1.0824	0.5571
0.1	Sphere	1.0935	1.0460	0.5351
	Total	1.0854	1.0511	0.4857
0.2	Ellipsoid	1.1445	1.2027	0.3188
0.2	Oblate	1.3326	1.3023	0.5737
0.2	Prolate	1.6617	1.6593	0.5214
0.2	Sphere	0.9882	0.9487	0.3338
	Total	1.2817	1.2217	0.5162

Note. For each row except the total, $N = 15$.

distribution. The mean value can be seen to decrease from 10%–20% to a few percent as grains get smaller. The total range of the deviations varies largely, and Q_{e1} ranges from 10^{-3} (10^{-4} for oblate spheroids) to 4×10^{-1}. The same is true for Q_{e2}, with even less variations between the different base shapes.

The range of difference from AMO in Figure 19 is considerably larger than that in LH07. This was already hinted in Figures 7 and 8, where the functional form of Q_{e2} is visibly more irregular than those presented in LH07. However, such behavior is natural when larger sets of randomly deformed irregular shapes are considered.

Third, in the AMO framework, RATs are not expected to depend strongly on the grain composition, but on grain helicity. Our calculations indeed show a similar magnitude of RATs for the different compositions.

Fourth, we consider the scaling predictions of torques given by the ensemble. The RAT magnitudes Q_Γ at $\Theta = 0$ were

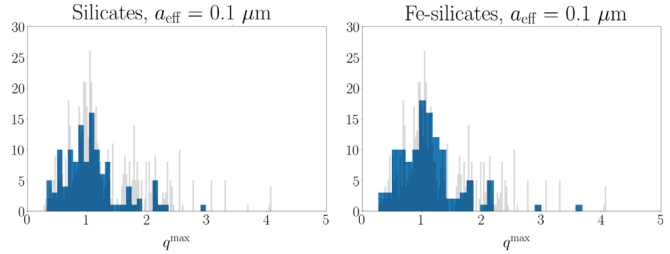

Figure 13. Comparison between $q^{\rm max}$ of 0.1 μm silicates with and without iron inclusions. The centers of distributions are approximately equal, with only slight differences between distributions.

calculated. Mean values and ranges of Q_Γ are presented in Figures 20–22. In all cases, self-similarity as reported in LH07 (e.g., Figure 30 in LH07) can be observed, though moreso in grains containing carbon. After a gradual steepening, the curves follow a power law closely proportional to $(\lambda/a_{\rm eff})^{-2.6}$. The power-law indices for each grain shape and composition are collected in Table 5. RAT magnitude scaling is weakly dependent on the grain shape or composition. Indices fall between -2.4 and -2.74, which gives slightly less steep fits than in the analysis in LH07, where a spectral index -3 provides the best fit for a severely more limited set of shapes. Therefore, while RAT scaling predictions can be done with a simple power-law estimate, our study suggests that a power-law index -2.6 should be used for a general fit.

Due to the limited wavelength range available, Figures 20–22 cannot show whether or not the RAT efficiency is best fitted by a constant below $\lambda/a_{\rm eff} = 1.8$, an estimate of the threshold between constant and power-law fits that originates from LH07. The region $\lambda \sim a_{\rm eff}$ is not possible to account for properly using the limited wavelength range. Due to this, the full RAT fit provided in LH07 cannot be confirmed for the ensembles.

Finally, we consider the precession-inducing RAT component Q_{e3}. From LH07, we know how to estimate Q_{e3} for the AMO spheroid, here chosen to have an aspect ratio $a{:}b = 2{:}3$, as

$$Q_{e3}^{\rm AMO} = -\frac{2e^3 a}{\lambda} K(\Theta, e)\sin 2\Theta, \tag{4}$$

where e is the spheroid eccentricity, a is its minor axis, and K is a fitting factor. For rough estimates of the maximum value $Q_{e3}^{\rm max}$, which are found at $\cos\Theta = \pm 2^{-1/2}$, LH07 showed that K is near unity. We study the wavelength-dependent normalized values of $\widehat{Q}_{e3}^{\rm max} = Q_{e3}^{\rm max}/Q_{e3}^{\rm max,AMO}$ for the silicate oblate and prolate ensembles. Using Equations (3) and (4) with $K \approx 1$, we also study the deviation from the estimated functional form of AMO.

The results, presented in Figure 23, reveal that there exists a critical value of $\lambda/a_{\rm eff} \approx 5$, where the maximal value and shape deviation against AMO of Q_{e3} are clearly anticorrelated, such that the maximum value of Q_{e3} is noticeably less and the shape is considerably different than what AMO predicts. Such a clear discrepancy against AMO was identified to be a property of only the Q_{e3} component. Above $\lambda/a_{\rm eff} \approx 5$, $\widehat{Q}_{e3}^{\rm max}$ quickly peaks, after which it gradually decreases. Also, below the critical value, another strong decrease is visible, although it is limited by the wavelength range used. That behavior, which is almost identical for the two different shape ensembles, can possibly be identified as being due to changing scattering regimes. To fully understand the universality of the critical grain size, which implies that in some situations certain grain size groups may exhibit a different types of alignment, further studies are needed.

5. Discussion

5.1. Importance of the Present Study

The absence of constraints on $q^{\rm max}$ in the theory of RAT alignment limits the predictive power of the theory. For instance, Figure 24 (see the gray shaded regions) indicates that for ordinary paramagnetic grains the high-J attractor point, and therefore perfect alignment of grains with magnetic field, is possible if the $q^{\rm max}$ parameter is above 2 for the angle between the radiation and the magnetic field $\psi < 45°$ and $q^{\rm max} < 1$ for $\psi > 45°$.

Our present study shows that for most grain shape distributions that we explored the most probable range of $q^{\rm max}$ is within 1.1–1.5 for large grains (see Section 4.2). This means that the observational detection of perfect alignment, e.g., by *Planck*[8] in this range necessarily implies that the alignment arises from the joint action of RATs and magnetic relaxation torques (see Hoang & Lazarian 2016; see the orange shaded region in Figure 24). Moreover, it can also constrain the magnetic response of the grain material (see Lazarian & Hoang 2018).

5.2. Role of q^{max} for Grains with Enhanced Magnetic Susceptibilities

The original model in LH07 has been significantly extended and elaborated in subsequent studies. Most important was the exploration of the joint action of the RATs and the enhanced magnetic relaxation first described in Lazarian & Hoang (2008, henceforth LH08) and numerically demonstrated in Hoang & Lazarian (2016, henceforth HL16). While the torques arising from paramagnetic relaxation within ordinary paramagnetic grains are completely negligible, the torques arising from the dissipation within a grain with an enhanced magnetic response, e.g., superparamagnetic grain (see Morrish 1980), are shown by LH08 to be important in stabilizing the high-J attractor point. Depending on the value of the parameter, $\delta_m = t_{\rm damp}/t_{\rm mag}$, where $t_{\rm damp}$ includes various grain randomization/damping processes (see Lazarian & Hoang 2018, and references therein), while $t_{\rm mag}$ is the time of the magnetic relaxation of a grain rotating perpendicular to the magnetic field direction, the parameter space for the $q^{\rm max}$ and the cosine of the angle between the magnetic field direction, and the radiation anisotropy direction, is changing as shown in Figure 2 from HL16. In the latter study, the range of $q^{\rm max}$ was unconstrained. However, in view of our present study we are able to show the ranges of parameters corresponding to the given classes of grain shapes.

Recalling that the alignment with low angular momentum corresponds to the alignment measure in the range of 20% or 30% (Hoang & Lazarian 2008, henceforth HL08), i.e., it is significantly reduced compared to the perfect alignment of

[8] In practice it may be easier to search for variations of the alignment degree with the angle between the magnetic field and the radiation anisotropy direction, as is done in Andersson et al. (2011). Within RAT theory the absence of variations of the alignment as revealed by Planck Collaboration et al. (2018) would indicate the perfect alignment of grains for all the angles and therefore the enhanced magnetic dissipation within grains.

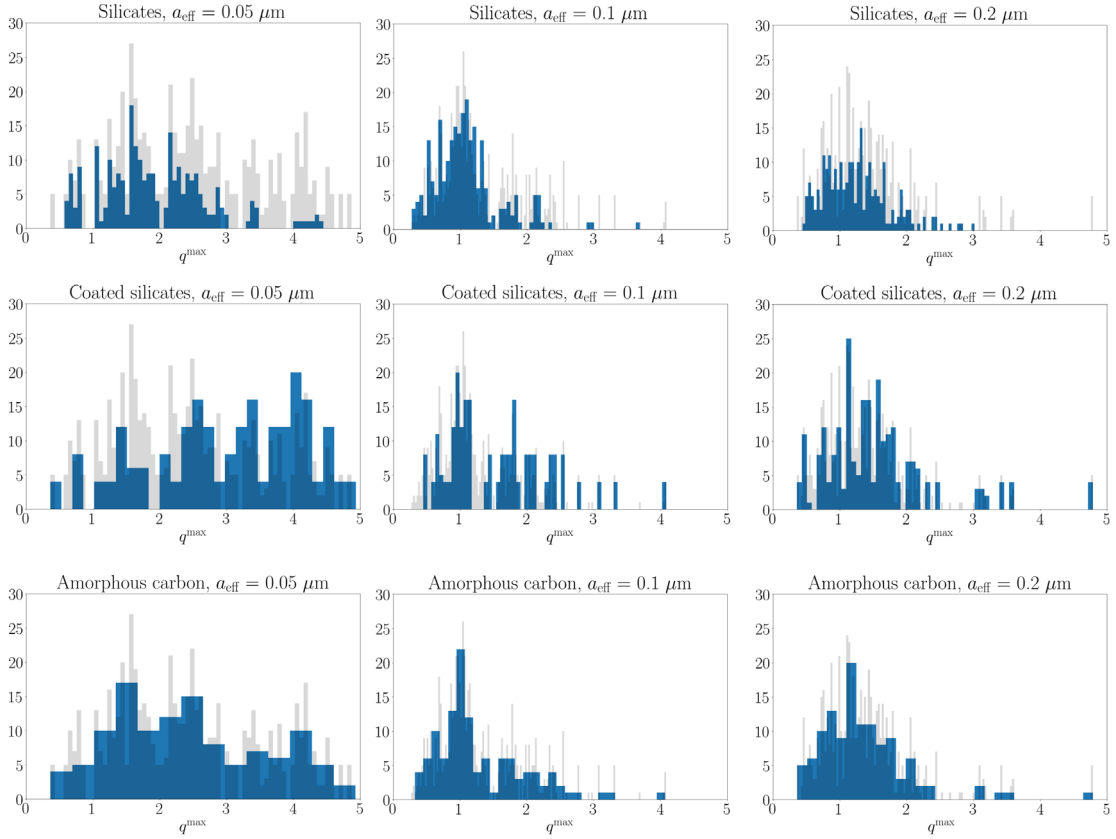

Figure 14. Comparison of $q^{\rm max}$ between composition groups of all sizes in the ISRF.

Table 4
Same in Table 2, but for the Three Different Composition Groups and with the Simplified ISRF Spectrum

Size(μm)	Composition	Mean	Median	STD	N
0.05	Silicate	1.9214	1.7963	0.7920	240
0.05	Coated	3.3230	3.3197	1.6573	240
0.05	Carbon	2.6158	2.4175	1.4760	120
	Total	2.6209	2.4186	1.4759	600
0.1	Silicate	1.0886	1.0466	0.4914	240
0.1	Coated	1.5437	1.4319	0.7470	240
0.1	Carbon	1.2968	1.0718	0.6679	120
	Total	1.3123	1.0942	0.6712	600
0.2	Silicate	1.2488	1.1923	0.4880	240
0.2	Coated	1.5360	1.4386	0.8031	240
0.2	Carbon	1.3485	1.2179	0.6651	120
	Total	1.3836	1.2920	0.6771	600

grains in the high-J attractor point,[9] one can see that the presence of a higher grain magnetic response can significantly increase the alignment measure.

HL16 performed detailed numerical studies for grains with varying levels of iron inclusions. HL16 derived the critical value of δ_m for which grains can be aligned with high-J attractors, and demonstrated that grains with high-J attractors

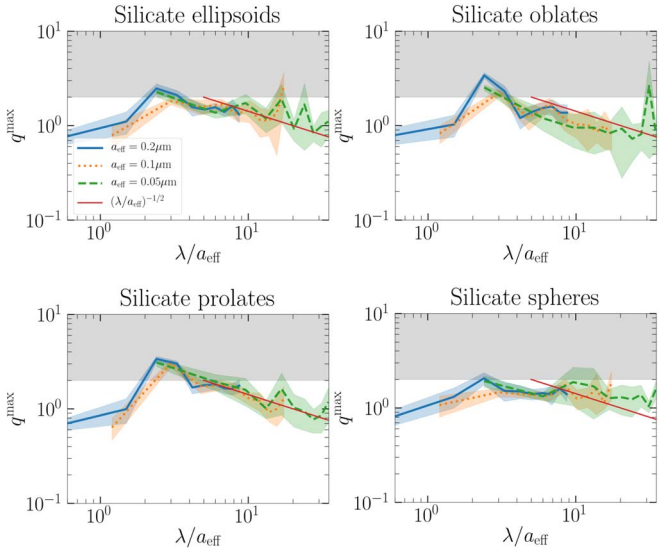

Figure 15. $q^{\rm max}$ as a function of $\lambda/a_{\rm eff}$ for the silicate base shapes. Each different grain size covers a different regime over $\lambda/a_{\rm eff}$, as the set of wavelengths is the same for all grain ensembles. The coefficient of variation is indicated by the shaded area around the mean. This statistic adequately corresponds to the amount of individual $q^{\rm max}$ values lying in and out of the darker area where high-J alignment is possible. The power-law fit is done for data between $\lambda/a_{\rm eff} = 2$ and 20.

can be perfectly aligned. Figure 24 shows the critical relaxation parameter that results in alignment with the high-J attractor where the middle region shaded orange corresponds to the most probable range of $q^{\rm max}$ computed from our grain ensemble. It shows that one only requires $\delta_{m,\rm cri} < 5$ to have alignment with

[9] The alignment is not close to zero (see Weingartner & Draine 2003) due to the gaseous bombardment that induces the diffusion of the phase trajectories of grains in the vicinity of the high-J repellor point (HL08).

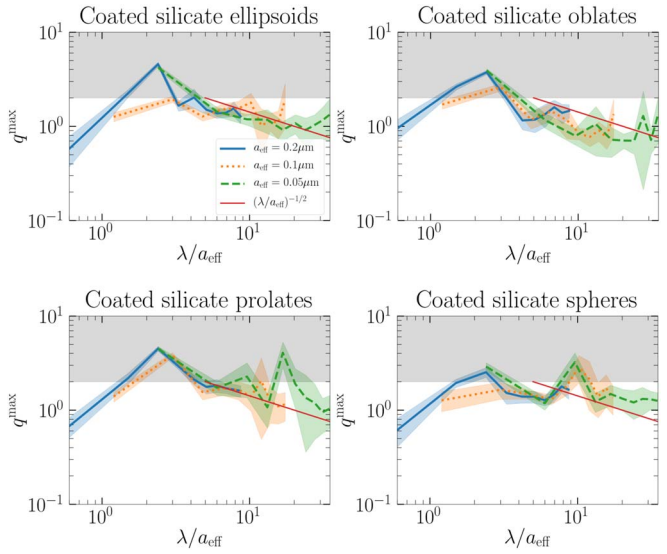

Figure 16. Same as for Figure 15, but for coated silicates.

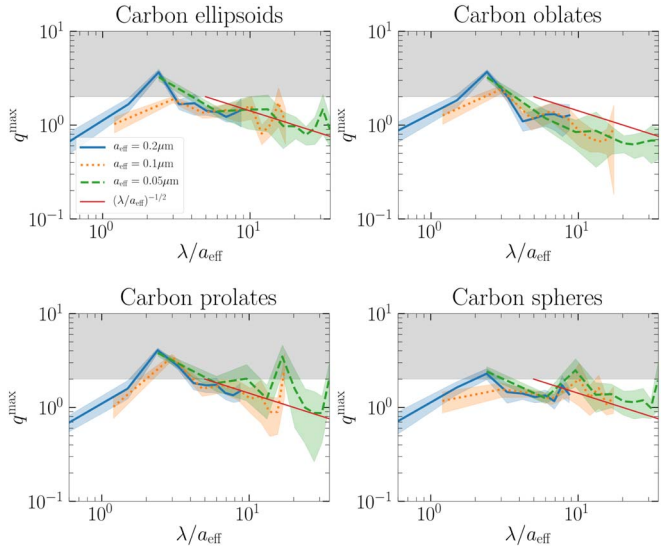

Figure 17. Same as Figure 15, but for carbonaceous shapes.

Table 5
Power-law Indices b Obtained from Least-squares Fits from Data between $\lambda/a_{\rm eff} = 2$ and 20 of the Form $y = ax^b$ for $q_{\max}$ (Figures 15–16) and $Q_\Gamma(\Theta = 0)$ (Figures 20–22)

	Ellipsoid	Oblate	Prolate	Sphere
$q_{\max}$(Silicate)	−0.168	−0.5702	−0.5275	−0.0798
$q_{\max}$(Coated)	−0.4739	−0.6322	−0.4675	−0.0857
$q_{\max}$(Carbon)	−0.4102	−0.6907	−0.4106	−0.143
Q_Γ (Silicate)	−2.6526	−2.6612	−2.7219	−2.7401
Q_Γ (Coated)	−2.43	−2.3991	−2.4768	−2.5778
Q_Γ (Carbon)	−2.4983	−2.4874	−2.5437	−2.6296

high-J attractors. This reveals that the magnetic susceptibility of grains is enhanced slightly to achieve perfect alignment.

Finally, an important quantity relating observations with RAT theory, the fraction $f_{\text{high-}J}$ of grains that are aligned with high-J attractors, can be considered in follow-up studies. The fraction depends on a number of parameters already available in this study, such as the grain size, its $q^{\max}$, and the radiative environment. In

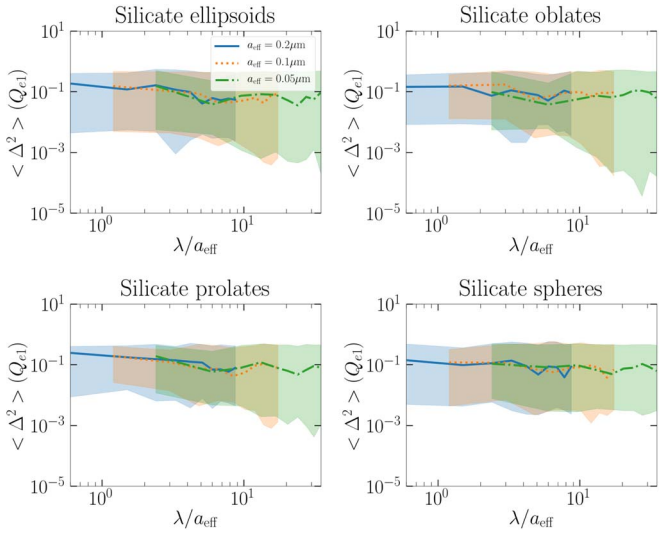

Figure 18. Mean deviation and range of the Q_{e1} component between each irregular silicate shape ensemble and AMO.

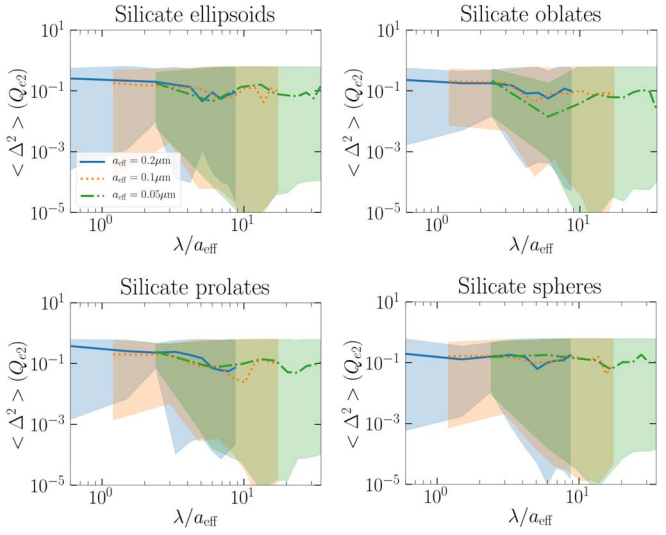

Figure 19. Same as Figure 18, but for the Q_{e2} component.

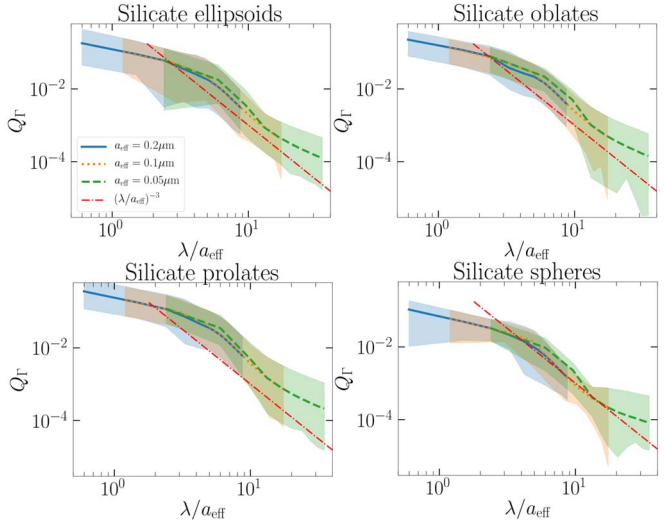

Figure 20. $Q_\Gamma(\Theta = 0)$ as a function of $\lambda/a_{\rm eff}$ for the silicate base shapes. The shaded area around the mean indicates the range of all samples. The power-law fit is done for data between $\lambda/a_{\rm eff} = 2$ and 20.

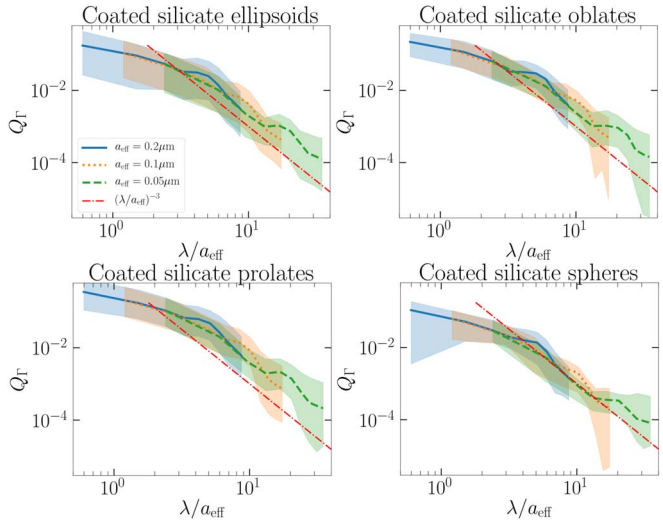

Figure 21. Same as Figure 20, but for coated silicates.

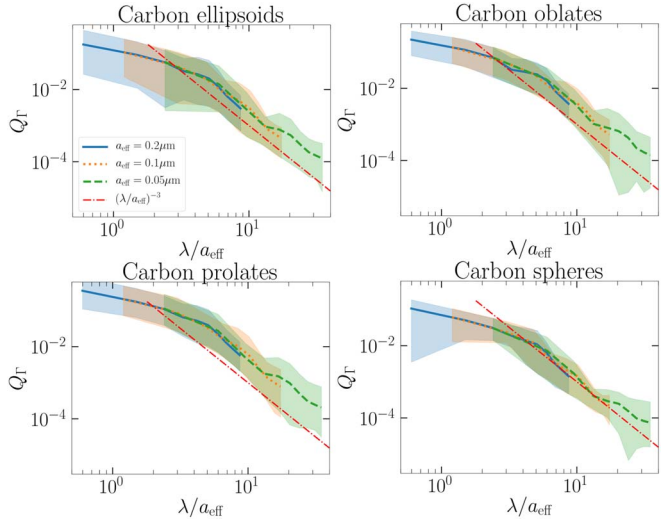

Figure 22. Same as Figure 20, but for carbonaceous shapes.

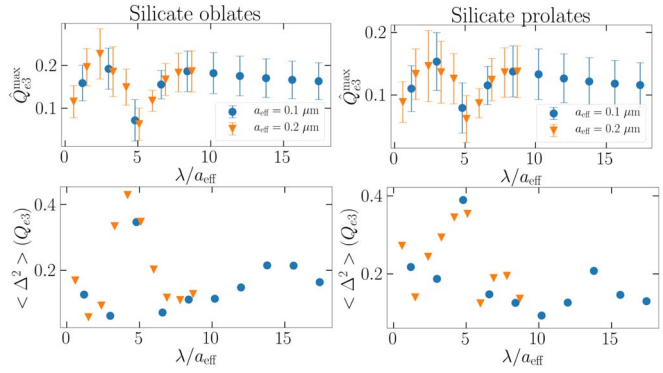

Figure 23. Top panels: mean values of the $\widehat{Q}_{e3}$ component, normalized with the corresponding AMO component, as a function of $\lambda/a_{\rm eff}$, for the silicate oblate and prolate ensembles. The bars represent 1 standard deviation around the mean. Below: mean deviation from AMO for the functional form, calculated using Equation (3). Strong anticorrelation between the top and bottom panels is visible near $\lambda/a_{\rm eff}\approx 5$, where the magnitude of $Q^{\rm max}_{e3}$ falls to near zero.

subsequent studies, by probing different ensemble properties of dust grains, more observationally relevant constraints are an important addition to current RAT theory.

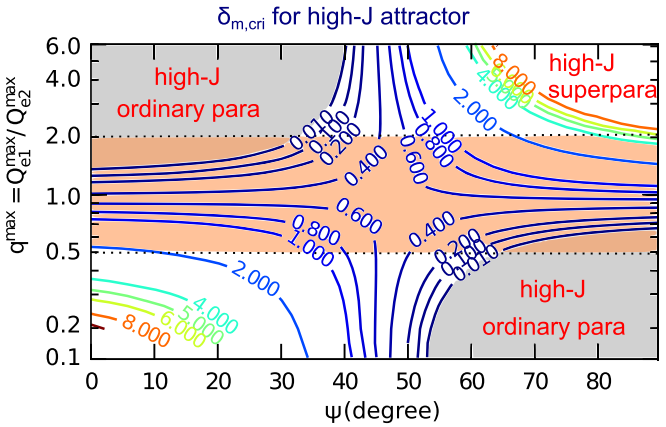

Figure 24. Critical magnetic relaxation parameter $\delta_{m,\rm cri}$ required to have alignment with a high-J attractor as functions of ψ and $q^{\rm max}$. The orange region marks the most probable range of $q^{\rm max}\sim 0.5$–2 computed for the ensemble of shapes.

5.3. Implication for RAT Alignment of Silicate versus Carbonaceous Grains

Our results show that RATs slightly vary with the composition of dust grains. RATs from carbonaceous grains are not much different from silicate grains. It follows that carbonaceous grains can also be spun up to suprathermal rotation by RATs as silicate and iron grains. As a result, the difference in grain alignment of different grain compositions originates from other physical properties, such as the grain magnetic properties. In the diffuse ISM, silicate grains can be aligned with the magnetic field due to fast Larmor precession. However, carbonaceous grains are not expected to be aligned with the magnetic field due to the rate of Larmor precession, which is lower than the rate of gas collisional randomization, assuming silicate and carbon grains are segregated perhaps due to rotational disruption by RATs (Hoang et al. 2018b). In dense molecular clouds, these two dust populations are mixed together due to grain collisions, thus, the composite silicate and carbon grains can potentially be aligned with the magnetic field.

5.4. Other Effects and the Uncertainties in the Alignment

In HL08 the role of suprathermal torques on the RAT alignment was explored. Such torques, e.g., arising from the H_2 formation on grain surfaces can raise the low-J attractor point, significantly increasing the composite (RATs + other uncompensated torques) alignment. This effect does not depend on the $q^{\rm max}$ parameter.

Other effects explored in earlier studies may also be important, but their role has not been properly quantified yet. For instance, the study that we provide is applicable to classical silicate grains of size less than 0.2 μm for which the internal relaxation (Purcell 1979; Lazarian & Draine 1999; Lazarian & Efroimsky 1999; Lazarian & Hoang 2018) efficiently aligns the axis of grain rotation and the axis of the maximal moment of grain inertia. For larger grains and also for carbonaceous grains this type of relaxation may not be sufficiently efficient. Then the grains wobble and may get aligned with the grain long axes both parallel and perpendicular to the magnetic field. The study in Hoang & Lazarian (2009) identified that internal relaxation of grains larger than 0.6–1.5 μm becomes inefficient, depending on the intensity of the radiation environment.

5.5. Other Types of Alignment

The alignment of grains can happen due to other processes that are different from the RATs. For instance, if the grain cross section is different with respect to the flow of particles or radiation, the "cross sectional" alignment take place (Lazarian & Yan 2005). This mechanism was employed recently in Hoang & Lazarian (2018) to explain the alignment of tiny aromatic carbonaceous grains (PAHs) in the vicinity of the radiation sources.

The concept of helical grain alignment was generalized to the corpuscular interaction with gaseous atoms (Lazarian & Hoang 2007b). The relative motion of grains and gas is expected due to turbulence (Lazarian & Yan 2002; Yan & Lazarian 2002; Yan et al. 2004; Hoang et al. 2011; Xu & Lazarian 2018). For the grain toy model (LH07: Figure 2), it does not matter whether the interactions are arising from the gas-grain or radiation-grain interactions. However, for realistic irregular grains the interactions are more complex. Unlike the radiation flow that samples the grain entirely and therefore determines the overall grain helicity, the grain helicity that is seen by the gaseous flow depends on the orientation of the grain rotation axes with respect to the flux of the impinging atoms. As a result, numerical simulations in Hoang et al. (2018a) demonstrate the shape of the torques that vary substantially and are not as universal, as in the case of the AMO in LH07. Due to variations of grain helicity as grains show different aspects of the flow, the amplitude of the mechanical torques on helical grains is also reduced. Nevertheless, such torques are more efficient compared to the stochastic mechanical torques associated with the Gold alignment (Gold 1952a, 1952b; Dolginov & Mytrophanov 1976b; Roberge & Hanany 1993; Lazarian 1994, 1995). A more extensive study of the mechanical alignment of helical grains is necessary, but our present approach of calculating the distribution of $q^{\max}$ for different grain shapes is not directly applicable in this case.

6. Conclusions

The present study analyzes the distribution of $q^{\max}$ parameter for a few classes of grain shapes that we believe can be present in astrophysical environments. In terms of the number of explored shapes, it presents a radical change, i.e., from 5 in LH07 and subsequent studies to 60 in the present study. We confirm that the RATs within the whole variety of shapes explored are consistent with the AMO model predictions in LH07. This, combined with the constrained values of $q^{\max}$ increase our confidence in the RAT theory and increase its predictive power. We found that superparamagnetic inclusions are important in order to have the perfect RAT alignment for a wide variety of shapes that we considered. Our study is important both for studies of magnetic fields in the interstellar medium as for probing physical conditions in other environments, e.g., comet atmospheres and circumstellar regions. In addition to testing the AMO model, we confirmed empirical relations for the scaling of RATs with the ratio of the grain size to the wavelength. These relations make it easier to evaluate the importance of the RAT alignment.

A.L. acknowledges the support by the NSF AST 1715754 grant. T.H. acknowledges the support from the Basic Science Research Program through the National Research Foundation of Korea (NRF), funded by the Ministry of Education (2017R1D1A1B03035359). Finally, all authors acknowledge the useful comments of an anonymous reviewer, which improved the manuscript considerably.

Appendix
Torque Efficiency Values via the *T*-matrix Method and DDSCAT

Calculated torque efficiencies Q_{ei} as functions of $\cos\Theta$ for 21 angles Θ and $\Phi = 0$, averaged over 20 angles β uniformly distributed in $[\pi/40, \pi(39/40)]$ about the grain rotational axis $\hat{\boldsymbol{a}}_1$ in Table 6. The DDSCAT geometries are composed from cubes each with $16 \times 16 \times 16$ dipoles, totaling 53,248 dipoles for

Table 6
Values of Q_{e1} and Q_{e2}, Calculated via the *T*-matrix Method Used in This Work and DDSCAT for Shapes 1 (Left Half) and 2 (Right Half), in Four Significant Figures, Respectively

cos Θ	Shape 1: Q_{e1}	$Q_{e1,\mathrm{DDSCAT}}$	Q_{e2}	$Q_{e2,\mathrm{DDSCAT}}$	Shape 2: Q_{e1}	$Q_{e1,\mathrm{DDSCAT}}$	Q_{e2}	$Q_{e2,\mathrm{DDSCAT}}$
−1.000e+00	1.250e-03	1.217e-03	−8.730e-16	4.762e-08	−2.960e-03	−3.025e-03	−5.560e-16	−1.905e-09
−9.000e-01	6.220e-04	6.003e-04	−1.690e-03	−1.682e-03	−1.770e-03	−1.816e-03	2.420e-03	2.376e-03
−8.000e-01	1.760e-04	1.637e-04	−2.130e-03	−2.128e-03	−8.620e-04	−9.014e-04	2.900e-03	2.838e-03
−7.000e-01	−1.340e-04	−1.375e-04	−2.280e-03	−2.277e-03	−1.870e-04	−2.188e-04	2.960e-03	2.899e-03
−6.000e-01	−3.430e-04	−3.412e-04	−2.230e-03	−2.240e-03	3.080e-04	2.818e-04	2.800e-03	2.740e-03
−5.000e-01	−4.820e-04	−4.748e-04	−2.050e-03	−2.064e-03	6.620e-04	6.412e-04	2.500e-03	2.442e-03
−4.000e-01	−5.700e-04	−5.601e-04	−1.770e-03	−1.785e-03	9.090e-04	8.907e-04	2.100e-03	2.047e-03
−3.000e-01	−6.240e-04	−6.116e-04	−1.410e-03	−1.424e-03	1.070e-03	1.054e-03	1.630e-03	1.583e-03
−2.000e-01	−6.550e-04	−6.414e-04	−9.980e-04	−1.007e-03	1.170e-03	1.151e-03	1.100e-03	1.072e-03
−1.000e-01	−6.700e-04	−6.572e-04	−5.420e-04	−5.475e-04	1.210e-03	1.192e-03	5.510e-04	5.310e-04
6.123e-17	−6.720e-04	−6.611e-04	−6.560e-05	−6.895e-05	1.210e-03	1.186e-03	−1.930e-05	−2.581e-05
1.000e-01	−6.630e-04	−6.546e-04	4.160e-04	4.140e-04	1.160e-03	1.135e-03	−5.890e-04	−5.825e-04
2.000e-01	−6.390e-04	−6.357e-04	8.850e-04	8.850e-04	1.060e-03	1.039e-03	−1.140e-03	−1.123e-03
3.000e-01	−5.950e-04	−5.963e-04	1.320e-03	1.325e-03	9.210e-04	8.915e-04	−1.660e-03	−1.632e-03
4.000e-01	−5.190e-04	−5.282e-04	1.710e-03	1.713e-03	7.210e-04	6.849e-04	−2.120e-03	−2.088e-03
5.000e-01	−4.000e-04	−4.168e-04	2.030e-03	2.025e-03	4.510e-04	4.090e-04	−2.510e-03	−2.465e-03
6.000e-01	−2.200e-04	−2.469e-04	2.240e-03	2.235e-03	9.940e-05	5.004e-05	−2.770e-03	−2.730e-03
7.000e-01	4.350e-05	6.248e-06	2.310e-03	2.304e-03	−3.490e-04	−4.051e-04	−2.880e-03	−2.838e-03
8.000e-01	4.190e-04	3.705e-04	2.190e-03	2.177e-03	−9.080e-04	−9.719e-04	−2.760e-03	−2.716e-03
9.000e-01	9.420e-04	8.805e-04	1.760e-03	1.741e-03	−1.590e-03	−1.663e-03	−2.240e-03	−2.206e-03
1.000e+00	1.660e-03	1.579e-03	2.580e-17	2.810e-07	−2.420e-03	−2.489e-03	−1.200e-16	−2.381e-08

shape 1 and 45,056 for shape 2. The tetrahedral discretizations for the *T*-matrix method are generated by discretizing models in OpenCAD. Shape 1 contains 19,968 tetrahedra, whereas shape 2 contains 1426 tetrahedra.

ORCID iDs

Joonas Herranen https://orcid.org/0000-0001-7732-9363
A. Lazarian https://orcid.org/0000-0002-7336-6674
Thiem Hoang https://orcid.org/0000-0003-2017-0982

References

Andersson, B.-G., Lazarian, A., & Vaillancourt, J. E. 2015, ARA&A, 53, 501
Andersson, B.-G., Pintado, O., Potter, S. B., Straižys, V., & Charcos-Llorens, M. 2011, A&A, 534, A19
Davis, L. J., & Greenstein, J. L. 1951, ApJ, 114, 206
Dolginov, A. Z., & Mytrophanov, I. G. 1976a, SvA, 19, 758
Dolginov, A. Z., & Mytrophanov, I. G. 1976b, Ap&SS, 43, 291
Draine, B., & Flatau, P. 1994, JOSAA, 11, 1491
Draine, B., & Lee, H. 1984, ApJ, 285, 89
Draine, B., & Weingartner, J. 1996, ApJ, 470, 551
Draine, B., & Weingartner, J. 1997, ApJ, 480, 633
Farsund, Ø., & Felderhof, B. 1996, PhyA, 227, 108
Gold, T. 1952a, MNRAS, 112, 215
Gold, T. 1952b, Natur, 169, 322
Hall, J. S. 1949, Sci, 109, 166
Herranen, J., Markkanen, J., & Muinonen, K. 2017, RaSc, 52, 1016
Herranen, J., Markkanen, J., & Muinonen, K. 2018, JQSRT, 205, 40
Hiltner, W. 1949, Sci, 109, 165
Hoang, T., Cho, J., & Lazarian, A. 2018a, ApJ, 852, 129
Hoang, T., & Lazarian, A. 2008, MNRAS, 388, 117
Hoang, T., & Lazarian, A. 2009, ApJ, 697, 1316
Hoang, T., & Lazarian, A. 2016, ApJ, 831, 159
Hoang, T., & Lazarian, A. 2018, ApJ, 860, 158
Hoang, T., Lazarian, A., & Draine, B. 2011, ApJ, 741, 87
Hoang, T., Tram, L. N., Lee, H., & Ahn, S.-H. 2019, NatAs, tmp, 319
Jones, A. P. 2012, A&A, 540, A2
Jones, A. P., Khler, M., Ysard, N., Bocchio, M., & Verstraete, L. 2017, A&A, 602, A46
Lazarian, A. 1994, MNRAS, 268, 713
Lazarian, A. 1995, ApJ, 451, 660
Lazarian, A. 2003, JQSRT, 79, 881
Lazarian, A., & Draine, B. T. 1999, ApJL, 520, L67
Lazarian, A., & Efroimsky, M. 1999, MNRAS, 303, 673
Lazarian, A., & Hoang, T. 2007a, MNRAS, 378, 910
Lazarian, A., & Hoang, T. 2007b, ApJL, 669, L77
Lazarian, A., & Hoang, T. 2008, ApJ, 676, L25
Lazarian, A., & Hoang, T. 2018, arXiv:1810.10686
Lazarian, A., & Roberge, W. 1997, ApJ, 484, 230
Lazarian, A., & Yan, H. 2002, ApJL, 566, L105
Lazarian, A., & Yan, H. 2005, in AIP Conf. Ser. 784, Magnetic Fields in the Universe: From Laboratory and Stars to Primordial Structures, ed. E. M. de Gouveia dal Pino, G. Lugones, & A. Lazarian (Melville, NY: AIP), 495
Markkanen, J., Ylä-Oijala, P., & Sihvola, A. 2012, ITAP, 60, 5195
Markkanen, J., & Yuffa, A. 2017, JQSRT, 189, 181
Morrish, A. H. 1980, The Physical Principles of Magnetism (Huntington: Krieger)
Muinonen, K., & Pieniluoma, T. 2011, JQSRT, 112, 1747
Ordal, M. A., Bell, R. J., Alexander, R. W., Long, L. L., & Querry, M. R. 1985, ApOpt, 24, 4493
Ordal, M. A., Bell, R. J., Alexander, R. W., Newquist, L. A., & Querry, M. R. 1988, ApOpt, 27, 1203
Ordal, M. A., Long, L. L., Bell, R. J., et al. 1983, ApOpt, 22, 1099
Planck Collaboration, Aghanim, N., Akrami, Y., et al. 2018, A&A, in press (arXiv:1807.06212)
Purcell, E. M. 1979, ApJ, 231, 404
Roberge, W. G., & Hanany, S. 1993, BAAS, 25, 1312
Scott, A., & Duley, W. W. 1996, ApJ, 105, 401
Spitzer, L., Jr., & McGlynn, T. A. 1979, ApJ, 231, 417
Waterman, P. 1965, IEEEP, 53, 805
Weingartner, J. C., & Draine, B. T. 2003, ApJ, 589, 289
Xu, S., & Lazarian, A. 2018, ApJ, 868, 36
Yan, H., & Lazarian, A. 2002, PhRvL, 89, 281102
Yan, H., Lazarian, A., & Draine, B. T. 2004, ApJ, 616, 895